Supplemental Document

Optics EXPRESS

Bendable long graded index lens microendoscopy: supplement

GUIGEN LIU,[1,8] JEON WOONG KANG,[2] SHARATH BHAGAVATULA,[1] SEBASTIAN W. AHN,[1] PETER T. C. SO,[2,3,4] GUILLERMO J. TEARNEY,[5,6,7] AND OLIVER JONAS[1,9]

[1] *Department of Radiology, Brigham and Women's Hospital, Harvard Medical School, Boston, MA 02115, USA*
[2] *Laser Biomedical Research Center, G. R. Harrison Spectroscopy Laboratory, Massachusetts Institute of Technology, Cambridge, MA 02139, USA*
[3] *Department of Mechanical Engineering, Massachusetts Institute of Technology, Cambridge, MA 02139, USA*
[4] *Department of Biological Engineering, Massachusetts Institute of Technology, Cambridge, MA 02139, USA*
[5] *Wellman Center for Photomedicine, Massachusetts General Hospital, Harvard Medical School, Boston, MA 02114, USA*
[6] *Harvard-MIT Division of Health Sciences and Technology, Cambridge, MA 02139, USA*
[7] *Department of Pathology, Massachusetts General Hospital, Harvard Medical School, Boston, MA 02114, USA*
[8] *gliu19@bwh.harvard.edu*
[9] *ojonas@bwh.harvard.edu*

Supplement DOI: https://doi.org/10.6084/m9.figshare.21120424

Parent Article DOI: https://doi.org/10.1364/OE.468827

Bendable long graded index lens microendoscopy: supplemental document

1. Supplemental Methods

1.1 Imaging system and data acquisition

The experimental setup shown in Fig. 1b was used for testing of imaging through the bendable long GRIN lens endoscope. The excitation laser was a pulsed laser source centred around 1040 nm with a spectral width of 16 nm (FemtoTrain 1040-3, Spectra-Physics), with a pulse width of < 370 fs, a pulse energy of > 350 nJ, and a peak power of >830 kW. A high-power optical isolator (ISO-FRDY-05-1030-W, Newport) prevented any reflected optical power from returning to the laser cavity. A variable beam splitter (VA5-PBS253, Thorlabs) functioned as a tunable attenuator for adjusting the laser power sent for imaging, and the other beam of the splitter was disposed of by a beam dump. The laser beam went through a 4f system constructed by a pair of tube lenses (TL1 and TL2), each with a focal length of 50 mm. A remotely controllable beam shutter (SHB1T, Thorlabs) placed after the 4f system blocked the excitation beam when necessary. Two galvanometer mirrors (GVS002, Thorlabs) provided the lateral (x and y) scans, which was followed by a beam size expansion system constructed through two tube lenses (TL 3 and TL 4) with a focal length of 50 mm and 200 mm, respectively. The expanded beam went through a dichroic mirror (FF705-Di01, Semrock) before it reached an electronically tunable lens (EL-10-30-TC-VIS-12D, Optotune) working in conjunction with an offset lens (LC4232, Thorlabs). The combination of tunable and offset lenses adjusted the convergence or divergence of the laser beam, and therefore the working distance of the objective (PLN 20x, Olympus). The working distance scan was used to implement depth (i.e., z) scan for the GRIN lens which was fixed by a lens holder and aligned with the objective. A camera pointed perpendicularly to the bend direction monitored the proximal end of the GRIN lens. The epi-reflected fluorescence signal was cleaned by the dichroic mirror and a bandpass filter. The bandpass filter was adjusted for different samples: for the doxorubicin solution, the filter had a center wavelength of 610 nm with a full width at half maximum (FWHM) of 10 nm (FB610-10, Thorlabs); for the fluorescent beads (T8880, ThermoFisher), the filter had a center wavelength of 531 nm with a FWHM of 22 nm (FF02-531/22-25, Semrock). The filtered optical signal was focused by a collimating lens (F950FC-A, Thorlabs) and sent to a photomultiplier tube (H7421-40, Hamamatsu) through a 1-m-long 1-mm-core MMF (FP1000ERT, Thorlabs) for image acquisition. A detailed description of the hardware for scan control and image acquisition can be found in our previous work [1]. For the bendable GRIN lens tested, a scan voltage ranging from -0.5 V to +0.5 V sent to the galvo mirrors led to a FOV of 162 μm in the x and y directions, and a driving current ranging from 14 mA to 29 mA sent to the tunable lens led to a scan range of 170 μm in the z direction. In all image postprocessing and display, a linear dependence of FOV on the scan voltage or current was assumed. All the 3D images had 100 X 100 X 100 voxels.

1.2 Lens deformation

In this work, the GRIN lens was subject to a cantilever beam-like deflection, as shown in Fig. 2b. For this type of deformation, only the section between l_s and l_e is curved, with its deflection v determined by [2]

$$v(l) = -\frac{V_e}{2L^3}(l-l_s)^3 + \frac{3V_e}{2L^2}(l-l_s)^2, \quad l_s \le l \le l_e, \tag{S1}$$

where $L = l_e - l_s$. The theoretical bend radius is given as [2]

$$R(l) = \frac{\left[1+\left(\frac{dv}{dl}\right)^2\right]^{\frac{3}{2}}}{\left|\frac{d^2v}{dl^2}\right|} = \frac{\left[1+\left(-\frac{3V_e}{2L^3}(l-l_s)^2 + \frac{3V_e}{L^2}(l-l_s)\right)^2\right]^{\frac{3}{2}}}{\left|-\frac{3V_e}{L^3}(l-l_s) + \frac{3V_e}{L^2}\right|}, \quad l_s \le l \le l_e. \tag{S2}$$

Note that at the bend end location, where $l = l_e$, the bend radius evaluates to infinity. We use Eq. (S2) substituted into Eq. (2) to simulate the ray trajectories within the bent section of the GRIN lens.

1.3 Numerical simulation of ray trajectories in the GRIN lens

As discussed in the Section 3 of the main text, the focal position of the GRIN lens may be tracked by the intersection point of ray trajectories within the meridional plane containing the center of the bend. The governing parameter is the ray invariant which is available for both the straight and bent sections of the lens, i.e., Eqs. (1) and (2). Since there is no analytical solution for the ray trajectory in the bent section, numerical simulation is used to track the ray paths. The simulation starts with the focused beam prior to entering the lens, as seen in Fig. 3c. Straight paths are assumed in all uniform media except the CL, RL, and IL because of their GRIN profiles which are available through the vendor. The refractive index (RI) profile is the same for both IL and OL, which reads

$$n(r) = 1.6289 - 1.509 \times r^2 + 1.154 \times r^4, \qquad 0 \le r \le \rho, \tag{S3}$$

and the RI profile of the RL is

$$n(r) = 1.6047 - 0.033 \times r^2, \qquad 0 \le r \le \rho. \tag{S4}$$

In Eqs. (S3) and (S4), r is measured in mm and the working wavelength is 1040 nm. In addition to the above RI profiles, other material RIs were used: 1.507 for the prism (provided by the vendor), RI of 1.4 for PDMS [3], and 1.33 for water (imaging in doxorubicin solutions).

As qualitatively shown in Fig. 3a, a ray bends as it travels along the bent section of the GRIN lens. As the ray travels toward the inner interface of the bend, it reaches a point $r = r_{ic}$, where the angle $\theta(r_{ic}) = 0$ (inner caustic). After reaching the inner caustic, the ray turns back and travels toward the outer interface. Again, the ray reaches a point $r = r_{tp}$, where $\theta(r_{tp}) = 0$ (turning-point caustic). Therefore, the ray bounces back and forth between the inner and tuning point caustics until it exits the bend. The values of r_{ic} and r_{tp} are solutions of r to [4]

$$(R + \rho)\overline{\beta} = (R + r)\left[n(r) + \Delta n(r)\right]. \tag{S5}$$

Because it is assumed that a ray is refracted and losses all its energy if it hits the lens interface (e.g., dashed curves in Fig. 5e), we are only interested in rays confined to the lens. Therefore, both r_{ic} and r_{tp} lie between $-\rho$ and ρ. When the lens is bent leftward, r_{ic} takes the smaller root; otherwise, it takes the larger root.

In all simulations, the whole lens (including the CL, RL, and IL, but excluding the side-view prism) is divided into two million axial sections (step size ~0.055 µm). The bent part of the lens is divided into multiple sectors with equal length, each sector is assumed to have a constant bend radius which is evaluated using Eq. (S2) at the proximal end of the sector. There are many axial sections of the same step size in each sector. The accuracy increases as the number of sectors increases (see Supplementary Figure S4), but with an increased computational cost. The bend was divided into 20 sectors in all our simulations, which was a good balance between accuracy and computational speed.

References

1. G. Liu, V. Valvo, S. W. Ahn, D. Thompson, K. Deans, J. W. Kang, S. Bhagavatula, C. Dominas, and O. Jonas, "A two-photon microimaging-microdevice system for four-dimensional imaging of local drug delivery in tissues," Int. J. Mol. Sci. **22**(21), 11752 (2021).
2. F. P. Beer, J. E. Russell Johnston, J. T. DeWolf, and D. F. Mazurek, *Mechanics of Materials* (McGraw-Hill, 2011), Chap. 9.
3. V. Prajzler, P. Nekvindova, J. Spirkova, and M. Novotny, "The evaluation of the refractive indices of bulk and thick polydimethylsiloxane and polydimethyl-diphenylsiloxane elastomers by the prism coupling technique," J. Mater Sci: Mater Electron. **28**, 7951-7961 (2017).
4. A. W. Snyder and J. Love, *Optical Waveguide Theory* (Chapman and Hall, 1983), Chaps. 1 & 9.

2. Supplemental Figures

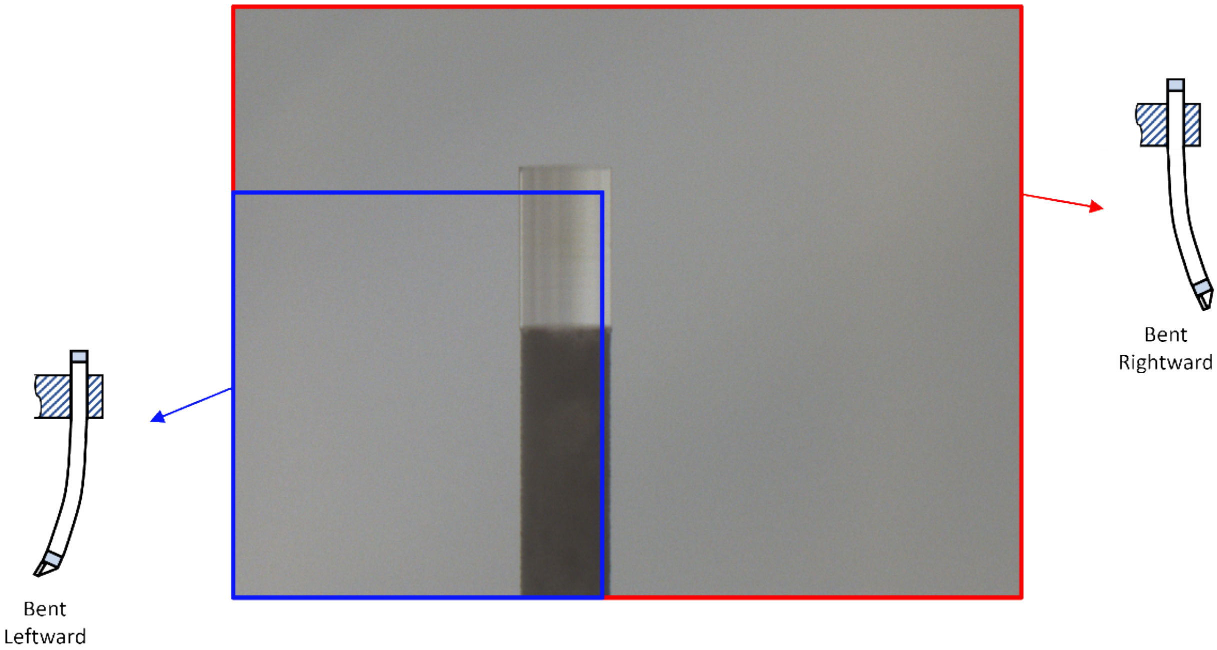

Supplementary Figure S1: Images of the lens top showing no visible displacement during the bending testing. Using the camera shown in Fig. 1b, the top part (proximal end) of the GRIN lens was monitored to check if it was displaced during the bending testing. Two images captured when the lens was bent rightward and leftward are stacked together. The bottom image with red edges was for the lens bent rightward ($l_s = 12.7\ mm$, $V_e = 1.75\ mm$) and the top one with blue edges was for the lens bent leftward ($l_s = 12.7\ mm$, $V_e = -1.75\ mm$). The top image was cropped toward the lower left corner till the lens in the bottom image was partially exposed. No visible displacement of the lens was observed between these two images. The lens diameter was 500 µm, the lens holder was made of ~3.2 mm thick and ~7.4 mm wide stainless steel, the tested lens bending was not strong enough to visibly deform the lens holder and thus the lens top was not displaced.

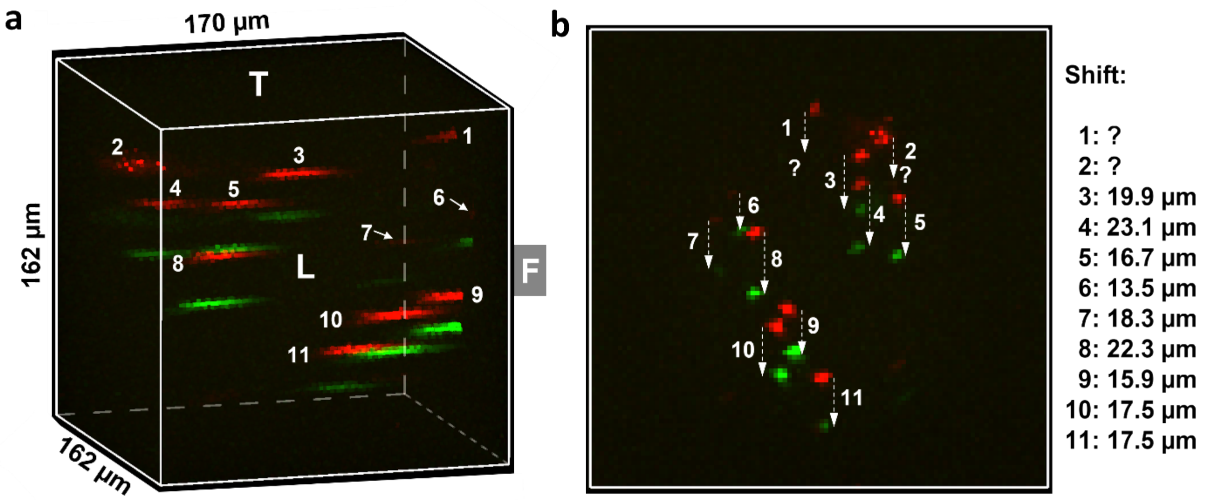

Supplementary Figure S2: Another testing of shift of bead positions across the FOV. (a) 3D view of the beads tested when the lens was straight (red) and bent leftward (green), (b) front view of bead positions and the measured shifts. These results suggest that the beads across the FOV shifted by similar amount, the minor difference is believed to come from experimental errors. This supplementary testing is to support that the shift is virtually uniform across the FOV, which is discussed in Fig. 5 and the according text of the main manuscript. Beads 1 and 2 were missing when the lens was bent leftward, which was due to the missing of Area 1 of the FOV shown in Fig. 5d. Experimental parameters: $l_s = 12.7\ mm$, $V_e = -1.75\ mm$.

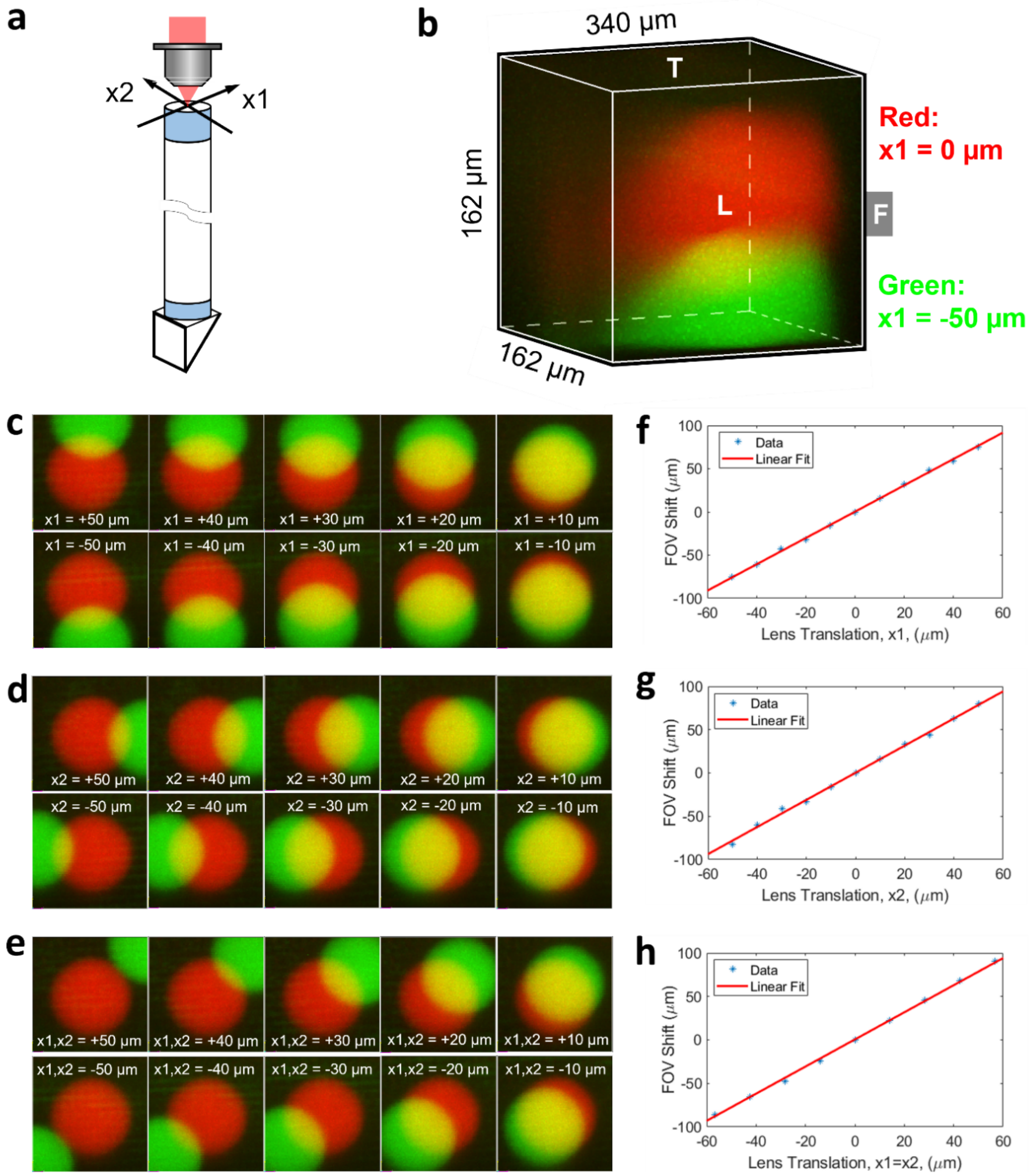

Supplementary Figure S3: FOV shift versus lens translation tested using a 1 mg/mL doxorubicin solution. (a) Schematic showing the directions of the lens translation, (b) an overlaid 3D image when the lens was at two different positions, (c)-(e) front view of FOV shift as the lens was translated toward different directions, (f)-(h) the measured FOV shift as a function of the lens translation. In all cases, the red image was for the lens at its original position (i.e., before translation). Slope of the linear fitting curve in (f)-(h) is 1.5235, 1.5674, and 1.5598, respectively, which corresponds to the object to image ratio of 1:0.66, 1:0.64, and 1:0.64, respectively. These values agree reasonably well with the nominal object to image ratio of 1:0.7 provided by the vendor. Also note that the lens translation does not change the shape of the FOV, which is opposed to the FOV deformation induced by the lens bending.

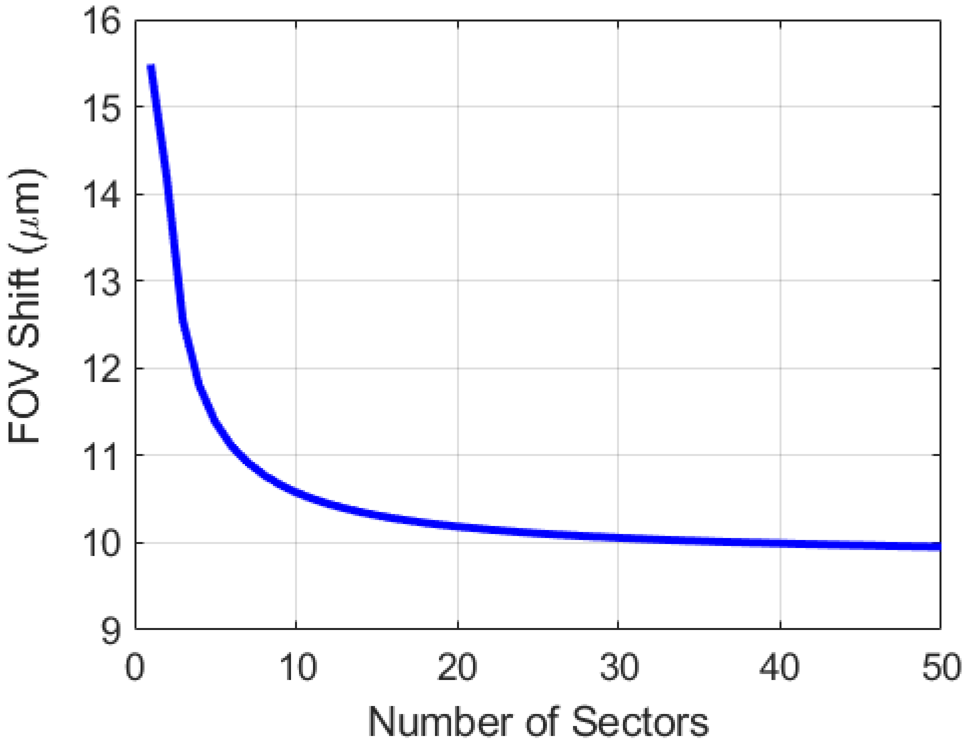

Supplementary Figure S4: Simulated FOV shift vs number of sectors of the bent section. The larger the number of sectors, the more stable (and more accurate) will be the calculated FOV shift.

3. Supplemental Table

Supplementary Table S1: Summary of resolution tested by all the three beads denoted in Fig. 4b of the main text.

Bent Leftward	Bead 1			Bead 2			Bead 3		
	x	y	z	x	y	z	x	y	z
Straight (R_s)	2.44	2.04	20.54	2.43	2.09	22.00	2.61	2.01	23.96
Bent (R_b)	2.31	2.27	23.05	2.54	2.51	24.69	2.64	2.06	24.40
$(R_b-R_s)/R_s$	-5.3%	11.2%	12.2%	4.5%	20.1%	12.2%	1.1%	2.4%	1.8%

Bent Forward	Bead 1			Bead 2			Bead 3		
	x	y	z	x	y	z	x	y	z
Straight (R_s)	2.35	1.95	20.45	2.36	2.12	21.81	2.62	2.05	23.83
Bent (R_b)	2.54	2.12	22.75	2.47	2.15	24.50	2.83	1.94	24.90
$(R_b-R_s)/R_s$	8.1%	8.7%	11.2%	4.6%	1.4%	12.3%	8.0%	-5.3%	4.5%